Unveiling the molecular environment of the ring nebula RCW 78

C. E. Cappa[1,2,★], M. Rubio[3], M. C. Martín[2,*], and G. A. Romero[1,2,4]

[1] Facultad de Ciencias Astronómicas y Geofísicas, Universidad Nacional de La Plata, Paseo del Bosque s/n, 1900 La Plata, Argentina
    e-mail: ccappa@fcaglp.fcaglp.unlp.edu.ar
[2] Instituto Argentino de Radioastronomía, C.C. 5, 1894 Villa Elisa, Argentina
[3] Departamento de Astronomía, Universidad de Chile, Casilla 36-D, Santiago, Chile
[4] Departamento de Física y Astronomía, Facultad de Ciencias, Universidad de Valparaíso, Chile

ABSTRACT

Aims. We present a study of the ionized, neutral atomic, and molecular gas associated with the ring nebula RCW 78 around the WR star HD 117688 (=WR 55) with the aim of analyzing the distribution of the associated gas and investigating its energetics.
Methods. We base our study on ^{12}CO(1–0) and ^{12}CO(2–1) observations of the brightest section of the nebula carried out with the SEST telescope with angular resolutions of 45″ and 22″, respectively; and on complementary ^{12}CO(1–0) data of a larger area obtained with the NANTEN telescope with an angular resolution of 2′.7. H I 21-cm line data taken from the ATCA survey, IRAS HIRES data, and radio continuum data at 4.85 GHz from the Parkes survey.
Results. We report the detection of molecular gas having velocities in the range –56 to –33 km s^{-1} associated with the western region of RCW 78. A few patches of molecular gas possibly linked to the eastern faint section are detected. The CO emission appears concentrated in a region of 23′ × 18′ in size, with a total molecular mass of $(1.3 \pm 0.5) \times 10^5$ $M_\odot$, mainly connected to the western section. The analysis of the neutral atomic gas distribution reveals the H I envelope of the molecular cloud, while the radio continuum emission shows a ring-like structure, which is the radio counterpart of the optical nebula. The gas distribution is compatible with the western section of RCW 78 having originated in the photodissociation and ionization of the molecular gas by the UV photons of the WN7 star HD 117688, and with the action of the stellar winds of the WR star on the surrounding gas. In this scenario, the interstellar bubble expanded more easily towards the east than towards the west due to the lack of dense molecular gas in the eastern section. The proposed scenario also explains the off center location of WR 55. A number of infrared point sources classified as YSO candidates showed that star formation activity is present in the molecular gas linked to the nebula. The possibility that the expansion of the bubble triggered star formation in this region cannot be discarded.

Key words. ISM: bubbles – ISM: individual objects: RCW 78 – stars: Wolf-Rayet – stars: individual: WR 55

1. Introduction

Interstellar bubbles created by the stellar winds of massive stars are generally detected as thermal radio continuum shells, as cavities and expanding shells in the H I 21-cm line emission distribution, and as shells in the far infrared (see Cappa 2006, for a summary). Radio observations allowed estimations of the electron densities and ionized masses for a number of galactic ring nebulae and identification of their neutral gas counterparts (e.g. Cappa et al. 2002).

The dense gas linked to these nebulae has been detected through molecular line observations. However, up to the present, only a few cases have been analyzed. These observations revealed the existence of large amounts of molecular gas and that photodissociation regions at the interface between the ionized and molecular gas and shock fronts are present in interstellar bubbles (Cappa et al. 2001; Rizzo et al. 2003).

In recent years, infrared images obtained from the MSX Galactic Plane Survey (Price et al. 2001) and GLIMPSE survey (IRAC images, Benjamin et al. 2003) have allowed us to investigate the distribution of the near- and mid-infrared emission associated with interstellar bubbles, confirming that PDRs and shock fronts are common phenomena linked to these

structures (Churchwell et al. 2006; Cyganowski et al. 2008; Watson et al. 2008, 2009).

Observational and theoretical studies, as well as numerical simulations, showed that only a small amount of the stellar wind energy released to the interstellar medium is converted into kinetic energy of the bubbles (see for example Chu et al. 1983; Oey 1996; Freyer et al. 2003, 2006; Cooper et al. 2004; Cappa 2006).

An important issue is the fact that the star formation process may be favoured in the compressed layers around the nebulae (Elmegreen 2000; Thompson et al. 2004). Using infrared point source catalogues, signs of star formation activity have been found in the dense molecular envelopes surrounding some interstellar bubbles (e.g. Cappa et al. 2005; Zavagno et al. 2007).

Thus, observations of molecular gas associated with interstellar bubbles provide information essential to investigating the energetics and star formation process in the dense surrounding shells.

Here we investigate the distribution of molecular gas associated with the optical ring nebula RCW 78 around WR 55 based on high angular resolution SEST observations, complemented with lower resolution data of the NANTEN telescope. Complementary IR, H I 21-cm line, and radio continuum archival data allow the analysis of the distribution of the ionized and neutral atomic gas, and that of the dust. Our aims are to

---

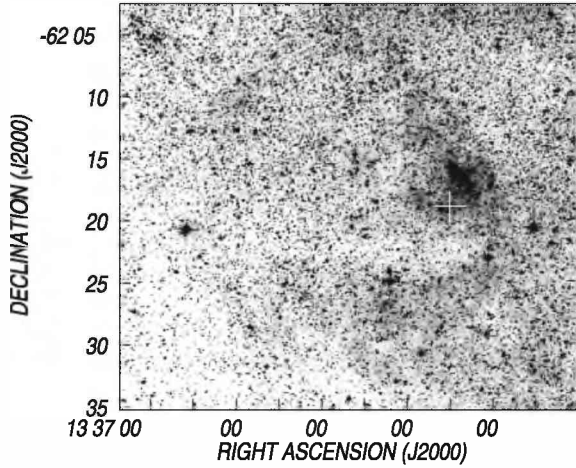★ Member of Carrera del Investigador, CONICET, Argentina.

Fig. 1. DSS-R image of the eastern and western sections of RCW 78. The cross indicates the location of the WR star.

identify and characterize the material linked to the ring nebula and to study its kinematics and energetics.

RCW 78 (=G 48b) is a ring nebula of about 35′ in diameter. The DSS-R image of the whole nebula is shown in Fig. 1, where the white cross marks the position of the WR star (see also Fig. 5 by Chu et al. 1983). The brightest part of RCW 78 is about 10′ × 6′ in size and offset to the northwest of the star, while fainter regions are present to the northeast, east, and south (Chu & Treffers 1981; see also Heckathorn et al. 1982). Chu (1981) classified the optical nebula as R_a because of its low expansion velocity and the lack of evidence for a shell structure in the velocity pattern of the bright regions. This last characteristic is explained by Chu & Treffers as due to the fact that the stellar winds have existed during a short period of time.

The Hα study by Chu & Treffers (1981) showed that the velocity of the ionized material spans from −38 to −53 km s^{-1}, varying from −44 km s^{-1} near the star to −53 km s^{-1} 7′ north of it. Georgelin et al. (1988) found a similar velocity of −41.4 km s^{-1} based on Hα Fabry-Perot data. Chu & Treffers (1981) explained the observed velocity pattern, which does not correspond to that of an expanding shell, as the consequence of an outflow caused by the ionization of the surface of the molecular cloud by the central WR star. Georgelin et al. (1988) found an additional component in the Hα line profiles at −24 km s^{-1}, most probably unrelated to the nebula.

Circular galactic rotation models (e.g. Brand & Blitz 1993) predict that gas with LSR velocities in the range −38 to −53 km s^{-1} lies at kinematical distances of 3.5–7.0 kpc. In this section of the Galaxy, the mentioned velocities are close to that of the tangent point, i.e. −48 km s^{-1}.

The study of the ionization structure by Esteban (1993) indicates that photoionization is the main source of excitation of the nebula, compatible with the clasification by Chu (1981).

The nebula is related to HD 117688 (=WR 55 = MR 49), a WN7 star located at $(l, b) = (307°48′, +0°9.6)$ or RA, Dec(J2000) = (13^{h}33^{m}30.1^s, −62°19′1.2″). Spectrophotometric distances d were estimated by several authors: 4.0 kpc (Georgelin et al. 1988), 5.5 kpc (Conti & Vacca 1990), 6.0 kpc (van der Hucht 2001). New NIR calibrations of absolute magnitudes in the K_s band by Crowther et al. (2006) indicate an absolute magnitude $M_{Ks} = −5.92$ mag for WN7-9 weak lined stars. Taking into account the K_s-value for WR 55 from the 2MASS catalogue (Cutri et al. 2003), and interstellar extinction values from Marshall et al. (2006), a distance in the range 4.5–5.0 kpc

can be derived. Based on the available distance estimates, we will adopt a distance of 5.0 ± 1.0 kpc for the WR star and its surrounding ring nebula.

The terminal wind velocity for WR 55 derived from the P Cyg profile of the CIV λ1550 line is in the range $V_w = 1000$–1200 km s^{-1} (Hamann et al. 1993; Rochowicz & Niedzielski 1995; Niedzielski & Skórzyński 2002). For the mass loss rate, Hamann et al. (1993) estimate log $\dot{M} = −4.2$ $M_\odot$ yr^{-1}.

In this paper, we present high angular resolution SEST observations performed in the ^{12}CO(1–0) and ^{12}CO(2–1) lines towards the brightest section of the nebula, complemented with lower angular resolution NANTEN data, H I 21-cm line data, radio continuum images, and infrared data of the whole region. In the next sections we describe the SEST data and analyze the distribution of the molecular, ionized, and neutral atomic emissions.

2. Data bases

2.1. CO data: observations and data reduction

The high resolution ^{12}CO(1–0) (115 GHz) and ^{12}CO(2–1) (230 GHz) data were obtained during two observing runs in 13–15 February 2002 and 20–21 March 2003, with the 15-m Swedish-European Submillimetre Telescope (SEST) at La Silla, Chile. The half-power beam-width of the telescope was 44″ and 22″ at 115 and 230 GHz, respectively. The data were acquired with the high resolution acousto-optical spectrometer, consisting of 1000 channels, with a total bandwidth of 100 MHz and a resolution of 40 KHz, corresponding to velocity resolutions of ≈0.105 km s^{-1} at 115 GHz [CO(1–0) line] and ≈0.052 km s^{-1} at 230 GHz [CO(2–1) line]. Calibration was performed using the standard chopper technique. The system temperatures were ≈400 K at 230 GHz and ≈320 K at 115 GHz. Pointing was checked once during each observing run on the SiO ($v = 1$, $J = 2 \rightarrow 1$) maser source Ori A. Pointing errors were 3″. The uncertainty in the intensity calibration was 10%. Details about the telescope and receivers can be found in Booth et al. (1989). The observed velocity intervals ranged from −70 to −10 km s^{-1} at 230 GHz and from −90 to +10 km s^{-1} at 115 GHz.

^{12}CO(2–1) and ^{12}CO(1–0) lines were acquired simultaneously in the position-switching mode on a grid with a spacing of 45″. The off-source position, at which no CO emission was detected, was placed at RA, Dec(J2000) = (13^{h}33^{m}10.3^s, −62°2′41″). The ^{12}CO observations were taken in the direction of 170 points towards the brighest section of the nebula and its environs. The observed positions are indicated by crosses in the SuperCOSMOS Hα image (Parker et al. 2005) shown in Fig. 2.

Aditionally, simultaneous ^{13}CO(2–1) and ^{13}CO(1–0) observations were carried out towards RA, Dec(J2000) = (13^{h}33^{m}10.7^s, −62°16′1″) and RA, Dec(J2000) = (13^{h}33^{m}10.91^s, −62°13′46″), two positions with strong ^{12}CO. The ^{13}CO data were acquired using the same 1000 channel high resolution spectrometer. The velocity resolution was 0.116 km s^{-1} at 110 GHz and 0.058 km s^{-1} at 220 GHz.

The spectra were reduced using the CLASS software (GILDAS working group)[1]. A linear baseline fitting was applied to the data, except in a few profiles where an order 3 polinomial was used. After smoothing the ^{12}CO profiles to a velocity resolution of 0.44 and 0.33 km s^{-1} at 115 and 230 GHz, respectively, the typical rms noise temperature was 0.22 K (T_{mb}) at 230 GHz and 0.11 K at 115 GHz after an integration time of 3 min. The rms noise temperature of the ^{13}CO(2–1) spectra was 0.20 K and
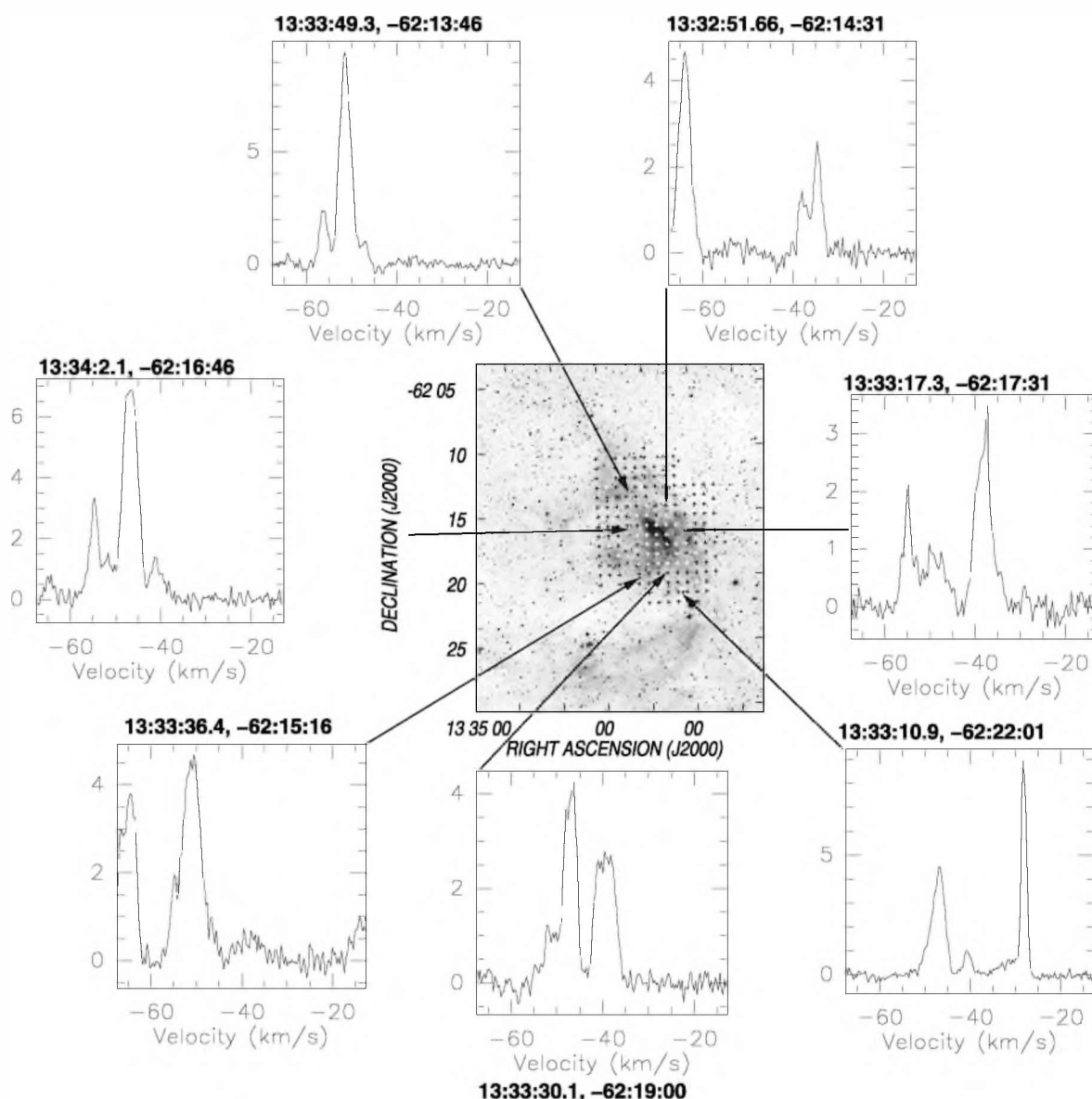
---

[1] http://www.iram.fr/IRAMFR/PDB/class/class.html

Fig. 2. *The central panel* displays the SuperCOSMOS Hα image of the W section of RCW 78. The grayscale is in arbitrary units. The crosses indicate the position of the 170 points observed in CO lines. The ^{12}CO(2–1) spectra corresponding to selected positions show molecular components with different velocities. The position of each spectrum is indicated. Intensities are given in main-beam brightness temperature.

0.10 K for ^{13}CO(1–0) after an integration time of 6 min. The spectra were smoothed to a velocity resolution of 0.46 km s^{-1} and 0.35 km s^{-1} at 110 GHz and 220 GHz, respectively.

The observed line intensities are expressed as main-beam brightness temperatures T_{mb}, by dividing the antenna temperature T_A^* by the main-beam efficiency η_{mb}, equal to 0.72 and 0.57 at 115 and 230 GHz, respectively (Johansson et al. 1998).

^{12}CO(2–1) and ^{12}CO(1–0) data cubes were constructed within AIPS software, which was used to perform most of the analysis.

2.2. Complementary data

Intermediate angular resolution ^{12}CO(1–0) data obtained with the 4-m NANTEN millimeter-wave telescope of Nagoya University corresponding to a region of 1°5 in size centered at RA, Dec(J2000) = (13^{h}35^m, −62°15′) were used to investigate the large scale distribution of the molecular gas in the environs of the whole RCW 78 nebula. The half-power beamwidth was 2′.6.

The 4 K cooled SIS mixer receiver provided typical system temperatures of ≈220 K (SSB) at this frecuency. The spectrometer was an acoustoptical spectrometer (AOS) with a velocity range of 100 km s^{-1} and a velocity resolution of 0.1 km s^{-1}.

The ionized gas distribution was analyzed using data at 4.85 GHz, extracted from the Parkes-MIT-NRAO (PMN) Southern Radio Survey (Condon et al. 1993). This survey was obtained with an angular resolution of 4′.2 and an rms noise of 10 mJy beam^{-1}.

To investigate the neutral atomic gas distribution we extracted H I data from the Southern Galactic Plane Survey (SGPS) obtained with the Australia Telescope Compact Array (ATCA) and the Parkes radiotelescope. A Hanning smoothing was applied to these data to improve the signal to noise ratio. The final data cube has a synthesized beam of 2′.4 × 2′.1, a velocity resolution of 1.64 km s^{-1}, and an rms noise of 1.0 K. A description of this survey can be found in McClure-Griffiths et al. (2005).

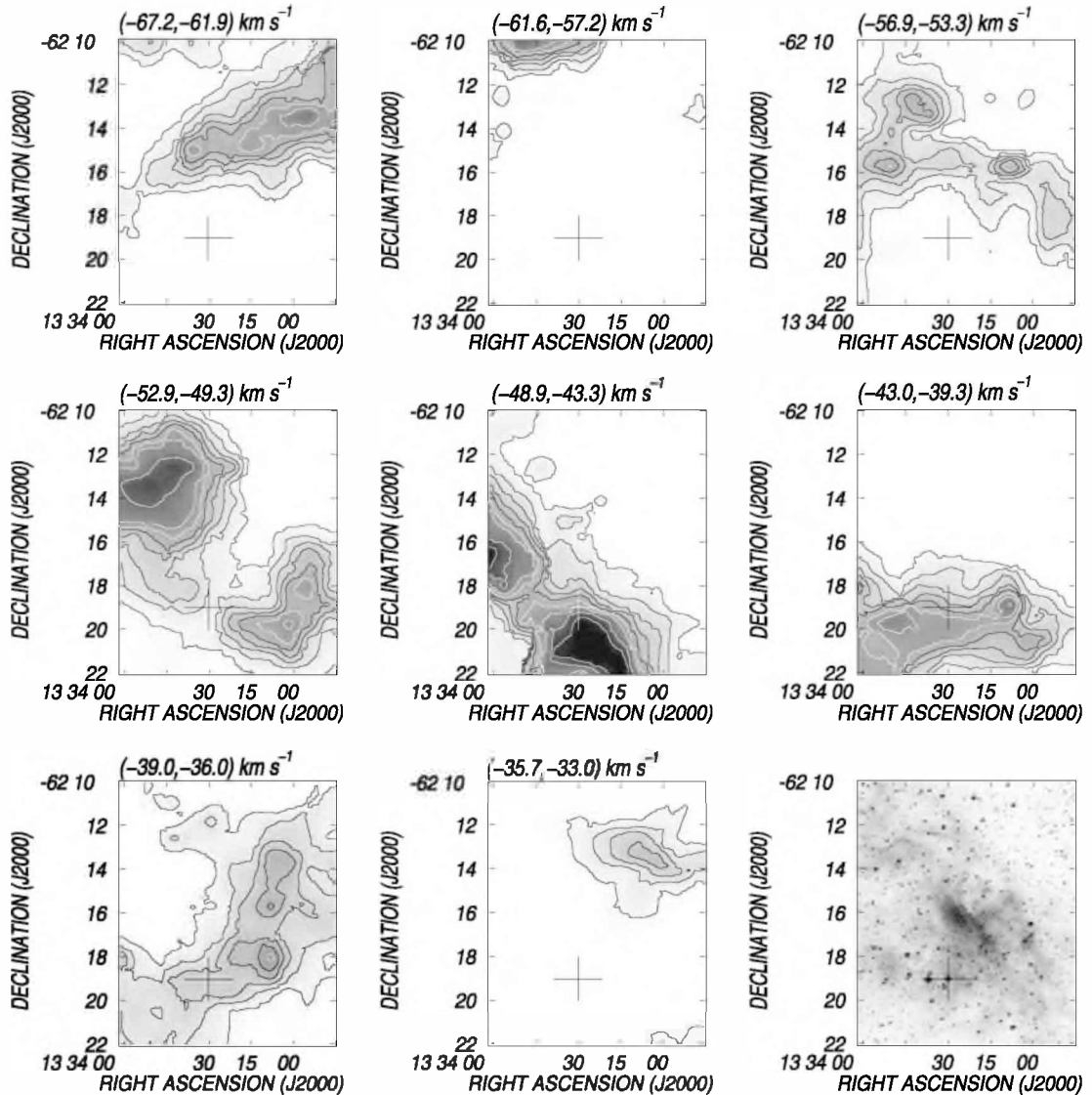The distribution of the IR emission was analyzed using high-resolution (HIRES) IRAS and MSX data obtained through

Fig. 3. Integrated emission of the CO(2–1) line within the velocity range from –67 to –33 km s^{-1} within selected velocity intervals. The grayscale is from 1 to 25 K km s^{-1}, and the contours are from 2.0 to 14.0 K km s^{-1} in steps of 2.0 K km s^{-1}, and 18.0 and 22.0 K km s^{-1}. *The bottom right panel* displays the SuperCOSMOS image for comparison. The cross marks the position of WR 55.

IPAC[2]. The IR data in the *IRAS* bands at 60 and 100 μm have angular resolutions of 1'.1 and 1'.9, respectively. The images in the MSX bands centered at 8.3, 12.1, 14.7, and 21.3 μm have an angular resolution of 18''.3. Images from the Spitzer mid-infrared data at 3.6, 4.5, 5.8, and 8.0 μm were obtained from the Galactic Legacy Infrared Mid-Plane Survey Extraordinaire (GLIMPSE, Benjamin et al. 2003) and retrieved from the Spitzer Science Center[3].

Finally, to search for star formation activity in the surroundings of WR55, we have inspected available IR point source catalogues: the MSX6C Infrared Point Source Catalogue (Egan et al. 1999) in Bands A (8.3 μm), C (12.1 μm), D (14.7 μm), and E (21.3 μm); the IRAS Point Source Catalogue[4] at 12, 25, 60, and 100 μm; and the IRAC point source catalogue, which includes photometry at 3.6, 4.5, 5.8, and 8.0 μm.

3. The distribution of the molecular gas

3.1. Analysis of the SEST data

Figure 2 displays CO(2–1) profiles obtained towards different sections of the nebula to illustrate the molecular components detected towards RCW 78. Within the observed velocity range, the CO profiles show molecular gas within the velocity interval –67 to –20 km s^{-1}. The main ^{12}CO components were detected at about –65, –50, and –40 km s^{-1}. Minor components detected in selected areas have velocities of around –55, –46, –35, and –28 km s^{-1}.

Figure 3 displays a series of images spanning the velocity range –67 to –33 km s^{-1} showing the distribution of the integrated emission of the CO(2–1) line within selected velocity intervals. The velocity intervals, which are indicated in the upper part of each image, were selected to emphasize the different CO velocity components. The bottom right panel shows the optical Hα image of the brightest section of the nebula. Components present at different velocities are described in the following paragraphs.

The CO emission distribution at velocities in the range −67.2 to −61.9 km s^{-1} shows an elongated cloud extending from E to W, beyond the surveyed area. Within the velocity interval from −61.6 to −57.2 km s^{-1}, the emission is concentrated towards the higher declination section of the image.

Molecular gas within the range −56.9 to −53.3 presents three intense clumps at RA, Dec(J2000) = (13^{h}33^{m}8^s, −62°15′45″), RA, Dec(J2000) = (13^{h}33^{m}42^s, −62°13′45″), and RA, Dec(J2000) = (13^{h}33^{m}48^s, −62°15′45″). A comparison with the optical image shows that the westernmost CO clump is located at the same position as a faint circular optical rim, suggesting that the borders of the CO clump are dissociated/ionized by the strong UV photon flux of the WR star. The CO emission is weak near the northern extreme of the brightest optical filament, whose W border is partially delineated by CO emission.

Gas in the interval from −52.9 to −49.3 km s^{-1} surrounds the brightest optical region all around except towards the NW. The CO emission is strong to the NE and SW.

Emission in the range −48.9 to −43.3 km s^{-1} surrounds the SE border of the brightest optical filament.

In the range −43.0 to −39.3 km s^{-1}, the emission is parallel to Dec(J2000) = −62°20′. This CO cloud coincides with a dust lane clearly seen in the Hα image. Note that the intense CO clump at RA, Dec(J2000) = (13^{h}33^{m}8^s, −62°19′) is projected to the southwest border of the brightest optical filament.

The emission in the range −39.0 to −36.0 km s^{-1} partially borders the W section of the brightest part of the nebula. The molecular emission at these velocities is also coincident with regions of strong absorption.

Finally, the image corresponding to the interval −35.7 to −33.0 km s^{-1} displays a cloudlet also coincident with the region of optical absorption to the northwest of the nebula.

The CO emission distribution in the whole velocity range and its comparison with the ionized gas indicates that the molecular material detected from −57 to −33 km s^{-1} is very probably associated with the nebula. We believe that CO emission present in the velocity range −67.2 to −61.9 km s^{-1}, which extends beyond the surveyed area and appears well separated in velocity from gas at $v > -57$ km s^{-1}, is unrelated to the nebula. Figure 4 shows the CO(2–1) integrated emission within the velocity range −57 to −33 km s^{-1} in grayscale and contours and an overlay with the SuperCOSMOS image for comparison. Clearly, the molecular gas emission is enhanced in the environs of the brightest region of RCW 78, encircling it. The comparison of the CO and optical emission distributions indicates that the nebula is interacting with molecular gas.

An inspection of Table 2 by Chu & Treffers (1981) shows that the velocities of the molecular gas are similar to those of the ionized gas: larger negative CO and Hα velocities are present to the N of the WR star, while lower negative CO and Hα velocities are detected close to and S of the star. The similar CO and H II velocities reinforces the association of the ionized and molecular gas.

3.2. Analysis of the NANTEN data

Figure 5 displays the distribution of the molecular gas in a larger area using data from NANTEN. The velocity range of each image has been selected to facilitate the comparison with the SEST images (Fig. 3). The rectangle indicates the area observed with SEST. In the following paragraphs we describe the NANTEN images, focusing first on the area observed with the SEST telescope, and then, extending the analysis to a larger area.
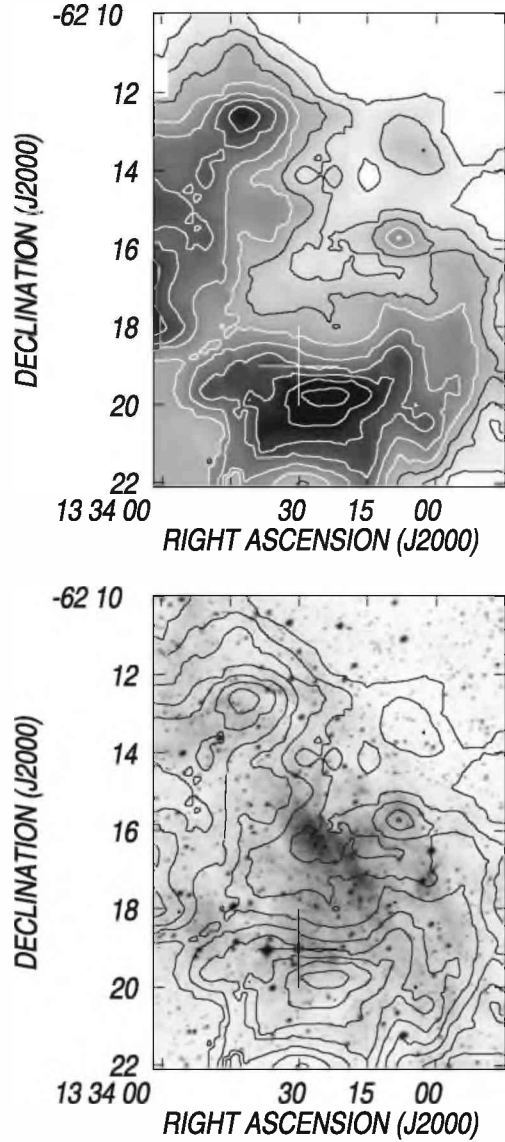

Fig. 4. *Top panel*: image showing the integrated emission of the CO(2–1) line within the velocity range from −56 to −33 km s^{-1}. The grayscale is from 8 to 50 K km s^{-1}, and the contours are from 10.0 K km s^{-1} to 50.0 K km s^{-1} in steps of 5.0 K km s^{-1}. *Bottom panel*: overlay of the CO contours of the top panel and the Super COSMOS image. The cross marks the position of WR 55.

The image corresponding to the velocity range −67.5 to −62.5 km s^{-1} shows an elongated CO cloud partially coincident with the brightest part of the nebula. The emission distribution indicates that this cloud is an extension of a larger one, which is present to the southeast of the WR star.

The emission in the intervals −61.5 to −56.5 km s^{-1} and −56.5 to −53.5 km s^{-1} shows little correlation with the optical emission.

The molecular emission in the range −52.5 to −49.5 km s^{-1} shows a CO arc-like structure which is almost coincident with the optical emission at RA(J2000) ≤ 13^{h}35^m. The intense CO clump centered at RA, Dec(J2000) = (13^{h}34^m, −62°15′) delineates the NE section of the brightest part of the nebula, while a fainter clump is detected to the SW, at RA, Dec(J2000) = (13^{h}33^{m}10^s, −62°21′). Both clumps, as well as the fainter CO emission region in between, are easily identified in the SEST images. This material is very probably related to RCW 78.
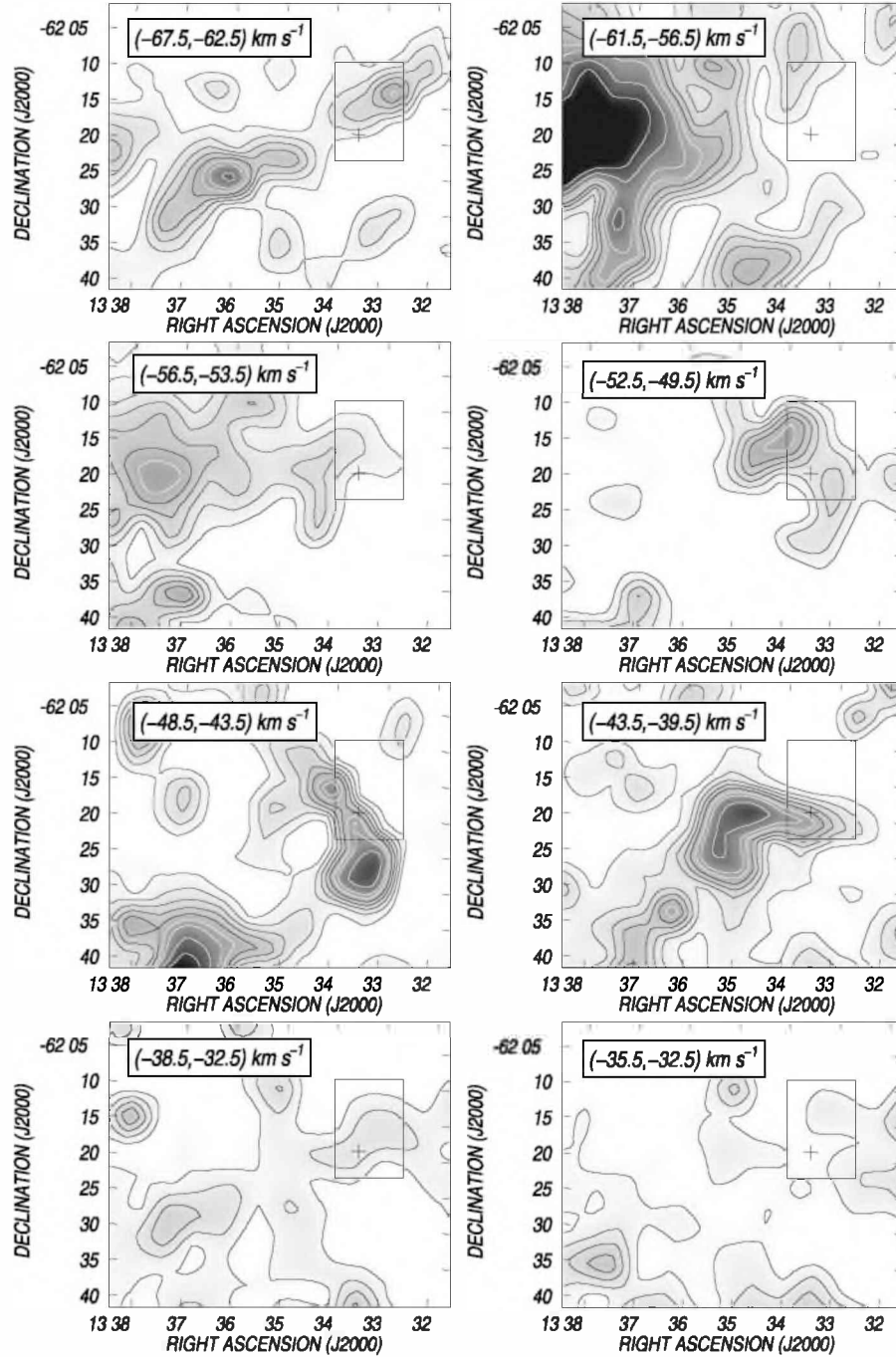
Fig. 5. Integrated emission of the CO(1–0) line within the velocity range from –67 to –33 km s^{-1} within selected velocity intervals, as obtained using the NANTEN telescope. The grayscale is from 1 to 25 K km s^{-1}, and the contours are from 2.0 to 14.0 K km s^{-1} in steps of 2.0 K km s^{-1}, and 18.0 and 22.0 K km s^{-1}. The rectangle indicates the region observed with the SEST, and the cross marks the position of WR 55.

The emission within the range −48.5, −43.5 km s^{-1} displays a CO feature from RA, Dec(J2000) = (13^{h}35^m, −62°10′) to (13^{h}33^m, −62°32′). The emission coincides with bright portions of the nebula and is shifted slightly towards the SW in comparison with the emission in the previous image. This characteristic is also observed in the image corresponding to the SEST data.

An elongated CO structure having velocities in the range −43.5 to −39.5 km s^{-1}, present at RA, Dec(J2000) = (13^{h}34^m, −62°20′), appears projected onto a dust lane at Dec = −62°22′. The molecular emission extends towards the south at RA(J2000) = 13^{h}35^m.

The CO emission is weak for velocities more positive than −38.5 km s^{-1}. Within the range −38.5 to −35.5 km s^{-1}, a

CO cloud is projected onto the nebula. The emission distribution changes for $v > −35.5$ km s^{-1}, where the CO emission coincides with regions showing faint optical emission.

In summary, the bulk of the molecular emission is concentrated in two structures having velocities in the range −52.5 to −43.5 km s^{-1} and −43.5 to −39.5 km s^{-1}, coincident with the velocities of the Hα line (Chu & Treffers 1981). Overlays of both features with the optical emission are presented in Fig. 6.

Based on morphological and kinematical evidence we can conclude that the arc-like structure having velocities in the range −52.5 to −43.5 km s^{-1} is clearly associated with RCW 78 (Fig. 6, left panel). As regards the feature with velocities from −43.5 to −39.5 km s^{-1} (Fig. 6, right panel), its velocity
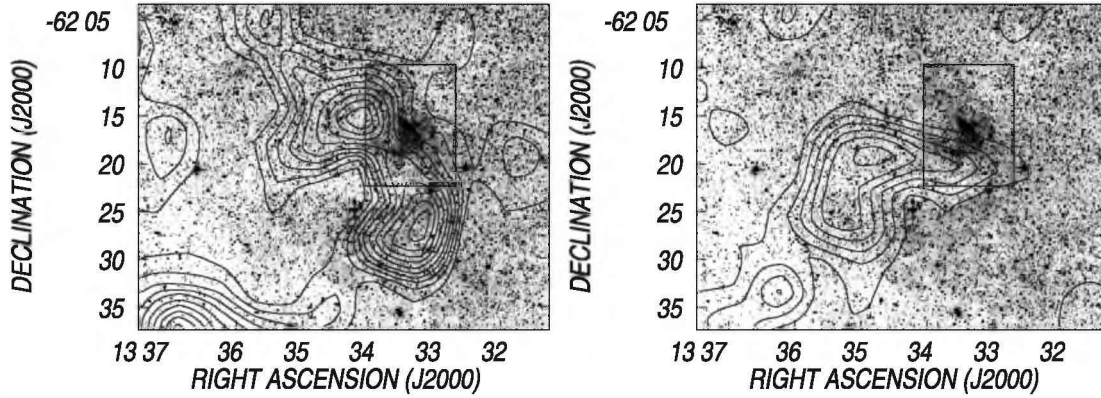
Fig. 6. *Left panel*: overlay of the DSS-R image and the integrated emission of the CO(1–0) line within the velocity range –56.5 to –43.5 km s^{-1} as obtained using the NANTEN telescope. The contours are 4.0 to 16.0 K km s^{-1} in steps of 3.0 K, and 20.0 to 40.0 K km s^{-1} in steps of 4.0 K km s^{-1}. *Right panel*: overlay of the DSS-R image and the integrated emission of the CO(1–0) line within the velocity range –43.5 to –39.5 km s^{-1} as obtained using the NANTEN telescope. The contours are 4.0 to 16.0 K km s^{-1} in steps of 3.0 K km s^{-1}, and 20.0 to 40.0 K km s^{-1} in steps of 4.0 K km s^{-1}. The rectangle and the cross have the same meaning as in Fig. 5.

is also coincident with those of the ionized gas, suggesting a relation to the nebula. On the contrary, material having velocities lower than –57 km s^{-1} does not seem to be related to the nebula.

CO emission linked to the eastern section of the nebula (near 13^{h}36^m) is difficult to identify. Molecular gas related to the eastern section is probably present in the range –43.5 to –38.5 km s^{-1} at RA, Dec(J2000) = (13^{h}36^m, –62°5′) and at RA, Dec(J2000) = (13^{h}37^m, –62°17′). However, the CO emission is weak, suggesting that the amount of molecular gas associated with this region is small compared with the western regions.

Both the SEST and NANTEN data in the environs of the western section of RCW 78 are consistent with a scenario in which the ionized gas originated through photodissociation and ionization of the parental molecular cloud. The lack of dense gas towards the east has probably favored the expansion of the ionized gas in this direction.

Adopting a mean radial velocity of around –45 km s^{-1}, circular galactic rotation models (e.g. Brand & Blitz 1993) predict near and far kinematic distances of 4.2 and 6.4 kpc, respectively, in agreement with the spectrophotometric distance of WR 55.

4. The associated ionized and neutral atomic gas

4.1. Ionized gas distribution

The upper panel of Fig. 7 displays the radio continuum image at 4.85 GHz in contours and grayscale. The location of the WR star is marked by the cross. The overlay of the optical and radio images shows that RCW 78 is detected at this frequency. The brightest section of the nebula coincides with one of the most intense radio continuum regions.

The brightest part of RCW 78 at RA, Dec(J2000) = (13^{h}33^{m}30^s, –62°17′) coincides with the brightest radio emission region. Comparison with the CO emission distribution shows that the intense radio emitting region is interacting with molecular material.

The radio continuum emission areas at RA, Dec(J2000) = (13^{h}34^{m}50^s, –62°27′) and RA, Dec(J2000) = (13^{h}36^{m}30^s, –62°15′) coincide with fainter optical emission regions. The region at RA, Dec(J2000) = (13^{h}33^{m}40^s, –62°22′), which lacks strong radio continuum emission, coincides with molecular gas having velocities in the range –43.5 to –39.5 km s^{-1} (see Figs. 2 and 4).
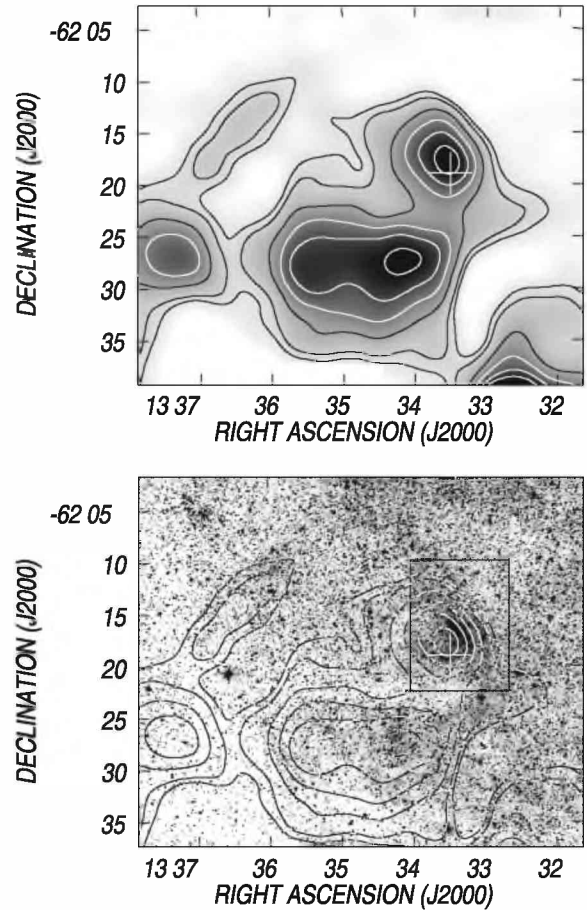

Fig. 7. *Top panel*: radio continuum image at 4.85 GHz. The grayscale is from –0.05 to 0.25 Jy beam^{-1}, and the contour lines are 30, 50, 100, 150, 200, and 250 mJy beam^{-1}. *Bottom panel*: overlay of the radio continuum image in contour lines and the DSS-R image. The rectangle delineates the region observed with SEST.

The strong radio emission region at RA, Dec(J2000) = (13^{h}37^{m}15^s, –62°27′), which is projected onto a region of strong absorption bordering faint optical areas belonging to RCW 78, is very probably unrelated.

The ring appearance of the radio continuum emission, which resembles the Hα emission distribution, is suggestive of the
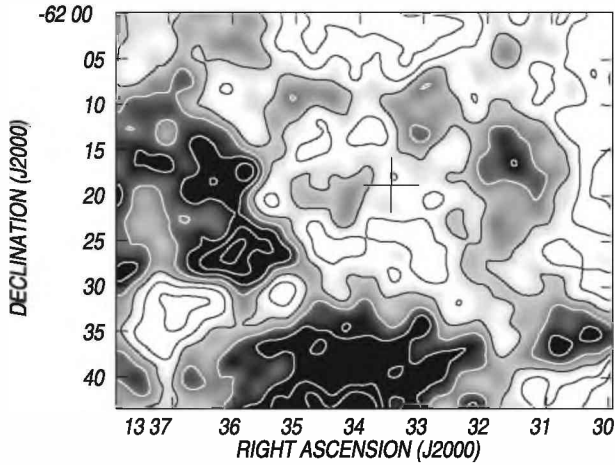
Fig. 8. Mean H I brightness temperature distribution within the velocity interval from −50.0 to −40.0 km s⁻¹. The grayscale is from 87 to 110 K, and the contour lines are from 80 to 110 K in steps of 5 K. The cross marks the position of WR 55.

action of the stellar winds of massive stars on the surrounding gas, which shaped an interstellar bubble. The ionized gas has probably expanded more easily towards the E than towards the W due to the lack of dense gas molecular gas in the eastern section. The proposed scenario also explains the off center location of WR 55.

4.2. H I gas distribution

The H I gas emission distribution in the range −55 to −25 km s⁻¹ is complex and clumpy, with few clear structures. Figure 8 displays the H I emission distribution within the velocity interval from −50 to −40 km s⁻¹ towards RCW 78.

The region of low H I emission centered at RA, Dec(J2000) = (13ʰ33ᵐ50ˢ, −62°23′) coincides with the western section of the nebula (shown in Fig. 1) and with CO emission having velocities in the range −52.5 to −39.5 km s⁻¹ (see Fig. 5), suggesting that most of the neutral gas in this region is H₂. In this scenario, part of the neutral atomic gas encircling the depression might correspond to the envelope of the molecular cloud.

4.3. Far IR emission

The HIRES IRAS image at 60 μm is shown in the upper panel of Fig. 9. The source at RA, Dec(J2000) = (13ʰ33ᵐ20ˢ, −62°17′) coincides with the brightest section of RCW 78, indicating the presence of dust mixed with the ionized gas. We will refer to this source as source A.

The region at Dec = −62°26′, from RA = 13ʰ32ᵐ30ˢ to 13ʰ36ᵐ, which depicts relatively strong far IR emission, coincides with an area showing optical emission. Two bright extended IR sources can be identified: one at RA, Dec(J2000) = (13ʰ34ᵐ15ˢ, −62°26′) (from here on referred to as source B), and the other at RA, Dec(J2000) = (13ʰ35ᵐ10ˢ, −62°26′) (source C). The sparsely populated open cluster C1331-622 and the star HD 117797 (RA, Dec(J2000) = 13ʰ34ᵐ12.0ˢ, −62°25′1″.8, O8Ib(f), Walborn 1982) are projected onto the line of sight to source B. C1331-622 is an open cluster of A and F-type stars placed at 820 pc, while the estimated distance for the O-type star is 3.9 kpc (Turner & Forbes 2005).
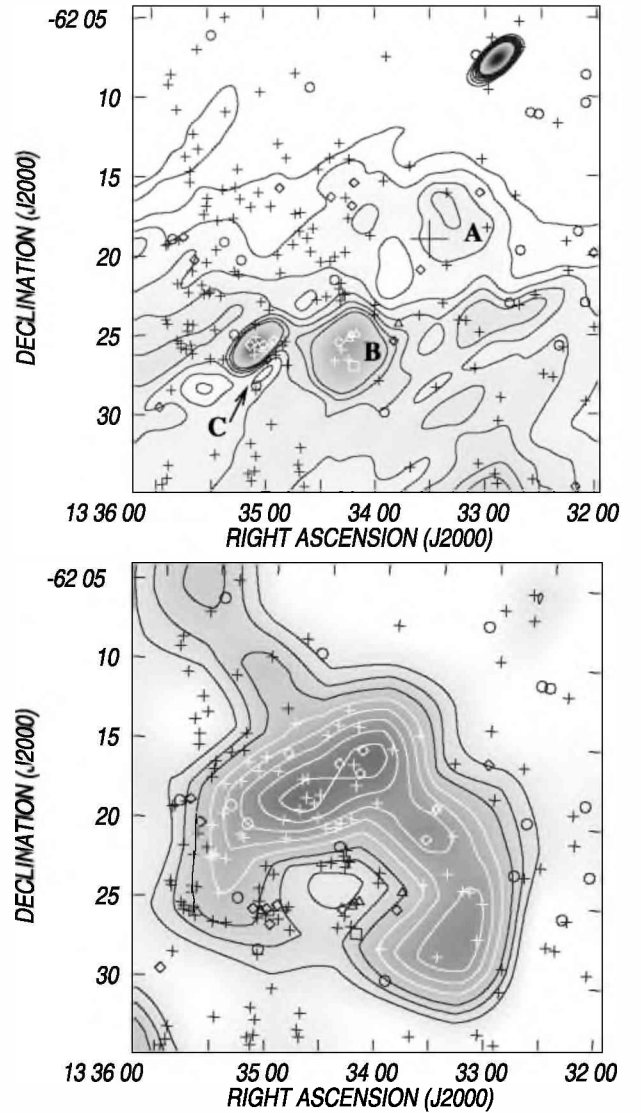

Fig. 9. *Upper panel*: distribution of the IR emission at 60 μm. The grayscale goes from 170 to 700 MJy ster⁻¹, and the contour lines are from 160 to 280 MJy ster⁻¹ in steps of 20 MJy ster⁻¹. Letters A, B, and C indicate infrared extended sources. *Bottom panel*: CO emission distribution within the velocity range from −56.5 to −39.5 km s⁻¹. The grayscale goes from 4 to 70 K km s⁻¹. The contours are 12, 16, 20, 25, 30, 35, 40, and 45 K km s⁻¹. The large cross indicates the position of the WR star. Small crosses, open circles, open diamonds, open triangles, and the square mark the position of YSO candidates.

Based on the IR fluxes at 60 and 100 μm, and following the procedure described by Cichowolski et al. (2001), we derived the dust color temperature for sources A, B, and C. Dust color temperatures are T_d = 29 ± 7 K, 44 ± 7 K, and 48 ± 6 K for sources A, B, and C, respectively. The range of temperatures for each source corresponds to $n = 1-2$ and to different IR background emission. The parameter n is related to the dust absorption efficiency ($\kappa_\nu \propto \nu^n$). The dust temperature derived for the far IR source related to the brightest region of RCW 78 (source A) is typical of H II regions. Estimates for sources B and C are clearly higher, probably revealing the presence of inner heating sources.

The IRAC image at 8 μm displays very faint extended emission towards the brightest section of RCW 78 (coincident with the IR source A), without identifiable structures. The emission

in this band towards IR sources B and C shows some weak small scale features which are difficult to characterize without high angular resolution molecular line data. The emission in MSX Band E (at 21.3 μm) shows a region of emission of about 2′ in size, centered at RA, Dec(J2000) = ($13^h34^m13^s$, $-62°25′$), approximately coincident with source B. Band E includes continuum emission from very small grains, which can survive inside ionized regions (cf. Deharveng et al. 2005, and references therein), and a contribution from nebular emission lines.

5. Star formation

To look for star formation activity in the surroundings of WR 55, we have inspected three different infrared point source catalogues: Spitzer, MSX, and IRAS. The study consisted of identifying candidates of Young Stellar Objects (YSOs) associated with the molecular gas in RCW 78. An area of 30′ × 30′ in size centered at RA, Dec(J2000) = (13^h34^m, $-62°20′$) was examined.

To identify YSO candidates in the IRAS and MSX catalogues, we followed the criteria of Junkes et al. (1992) and Lumsden et al. (2002), respectively.

A total number of 20 IRAS point sources were found projected onto the analyzed region. Eight out of the 20 sources have IR fluxes compatible with protostellar objects, and only 1 of them is projected onto the molecular gas related to the nebula.

Lumsden et al. (2002)'s conditions were used for MSX sources. The selection of candidates was performed taking into account their loci in the (F_{21}/F_8, F_{14}/F_{12}) diagram. Their criteria allow identification of candidates of massive young stellar objects (MYSOs) and compact H II regions (CHII). A total of 16 MSX sources are projected onto the whole region. Two sources classified as CHII and 2 MYSO candidates are seen projected onto the molecular material associated with RCW 78.

To search for YSO candidates, we also analyzed the mid-infrared emission of point sources using Spitzer IRAC photometry. This data base provides excellent tools for identifying and classifying YSO candidates as Class I and II. We investigated the infrared excess by measuring the infrared spectral index α_{IR} (=dlog(λF_λ)/dlogλ) (see Lada 1987; Stahler & Palla 2005; Chavarria et al. 2008; Koenig et al. 2008).

Within the selected region, we found 5860 sources with detections in the 6 bands (H ans K_S, from the 2MASS catalog, and the four IRAC bands). To deredden the magnitudes, we estimated the extinction using the 2MASS ($H - K_S$) colors in areas of about 2′ in size following the method described by Lada et al. (1994). The extinction laws are from Rieke & Lebofsky (1985) and Flaherty et al. (2007) for the 2MASS and IRAC bands, respectively.

To select young candidates, we took into account sources having spectral index α_{IR} in the range -1.5 to $+2$ for each pair of IRAC wavelengths. Starburst galaxies and active galactic nuclei were removed from the sample by using the color–color diagram [3.6]–[4.5] vs. [4.5]–[8.0] from Simon et al. (2007). We applied a second selection criterion to the remaining sources, taking into account sources with ($K_s - [4.5]$) > 0.4, following Koenig et al. (2008). After inspecting visually the SEDs of the remaining sources, we were left with 193 YSO candidates. Note that two selection criteria were applied. This procedure is quite strict and we are aware that a number of YSO candidates have probably been rejected. However, selected sources are more confident candidates.

Finally, we used the IR spectral index to discriminate Class I sources ($0 < \alpha < +2$) from the more evolved

Class II sources ($-1.5 < \alpha < 0$). Sources with a nearly flat IR spectral distribution ($\alpha \simeq 0$) were named Class I-II.

The distribution of the YSO candidates identified using the IRAS, MSX, and Spitzer data bases is shown in Fig. 9, overlaid onto the 60 μm and the CO emissions. Note that the CO emission shown in the figure includes molecular gas at two different velocities (from -56.5 to -43.5 km s^{-1}, and from -43.5 to -39.5 km s^{-1}). The symbols used in the figures have the following meaning: the open square marks the position of the IRAS point source, open circles indicate Class I objects; small crosses, Class II objects, diamonds Class I-II objects, and open triangles correspond to CHII and MYSOs.

The spatial distribution of the candidates is not uniform. About 120 sources are projected onto the molecular gas, mainly concentrated towards RA(J2000) > 13^h34^m. A relatively large number of YSO candidates are projected bordering the low CO emission region centered at about RA, Dec(J2000) = ($13^h34^m30^s$, $-62°25′$). Two areas in this region are particularly interesting: one at RA, Dec(J2000) = ($13^h34^m15^s$, $-62°25′$) and the other at RA, Dec(J2000) = (13^h35^m, $-62°26′$), which include 22 sources. These sources are listed in Table 1. Their main parameters (coordinates, fluxes) as well as an indication of the nature of the sources are included in Table 1.

The upper panel of Fig. 9 shows that both groups of YSO candidates coincide with the IR extended emission regions named B and C (see Sect. 4.3). The MSX sources #2, #4, and #5, the Spitzer sources #6, #7, #8, and #9 match the location of the IR source B. In particular, MSX sources #2 and #4 approximately coincide in position with the extended source detected in Band E and with the O8Ib(f) star HD 117797. The presence of this collection of point sources suggests the existence of an active star forming region. The region of extended emission in Band E, which is most probably related to a compact H II region in that direction, reinforces this suggestion. Note that the O8Ib(f) star HD 117797 is projected onto the borders of the bright sections of the molecular clouds, indicating that the dense material has probably been dissociated by the UV photons of this massive star.

The position of MSX point source #3 and the Spitzer sources #10 to #22 coincide with the extended IR source B (at RA, Dec(J2000) = ($13^h35^m15^s$, $-62°26′$), indicating the detection of an additional stellar forming region. The source IRAS 13316-6210 (RA, Dec(J2000) = ($13^h35^m2^s$, $-62°25′30″$), whose IRAS fluxes do not match Junkes et al.'s criteria, is also coincident with this region.

In Fig. 10 we plot the dereddened color–magnitude diagram for the YSO candidates detected using the Spitzer database, which appear related to the IR sources B and C, i.e. those listed in Table 1. A distance of 5 kpc was assumed. We compare the position of the YSO candidates with the main sequence stars from B3V to O3V, and with an isochrone calculated by Siess et al. (2000) corresponding to an age of 1 Myr (dot line). The K_s-limit of our sample is about 14 mag, which corresponds to a limit in the absolute magnitude of K_S of about 0.5 mag and to pre-main sequence stars with masses higher than about 2.2 $M_\odot$ in the Siess et al. model. This diagram suggests that the YSOs candidates in both selected regions have masses higher than this last value. Note, however, that as their luminosity originates both in the central object and in the circumstellar material, the effective mass of the candidates may be lower than estimated (Comeron et al. 2005).

Sub-millimetre continuum observations would be useful to confirm the nature of the YSO candidates.

Table 1. YSO candidates projected onto the infrared extended sources B and C (near RA, Dec(J2000) = [13^{h}34^{m}30^s, −62°25′]).

#	l[h m s]	b[° ′ ″]	IRAS source	Fluxes[Jy]						Class.
				12 μm	25 μm	60 μm	100 μm			
1	13 34 11.4	−62 27 03	13307-6211	0.8	2.0	20.5	85.4			YSO/Class 0
#	l[h m s]	b[° ′ ″]	MSX source	Fluxes[Jy]						Class.
				8 μm	12 μm	14 μm	21 μm			
2	13 34 13.0	−62 25 07	G307.8603+00.0439	0.2261	1.809	1.118	1.391			CH II, HD 117797
3	13 35 03.6	−62 25 77	G307.9563+00.0163	0.7808	0.7287	0.5542	3.093			CH II
4	13 34 10.2	−62 25 00	G307.8561+00.0463	0.2149	1.144	2.191	4.793			MYSO, HD 117797
5	13 34 13.8	−62 25 29	G307.8620+00.0399	0.1614	1.146	1.726	4.996			MYSO
#	l[h m s]	b[° ′]	GLIMPSE source	Fluxes[mag]						
				H	K_s	[3.6]	[4.5]	[5.8]	[8.0]	Class.
6	13 34 14.4384	−62 26.5794	G307.8597+00.0185	13.244	11.95	11.237	11.137	10.873	10.895	II
7	13 34 17.9136	−62 25.9506	G307.8680+00.0277	12.459	11.257	10.338	10.419	10.242	10.243	II
8	13 34 19.4304	−62 25.506	G307.8721+00.0345	11.202	9.599	7.489	7.385	6.928	6.641	I-II
9	13 34 21.564	−62 26.6934	G307.8729+00.0143	13.959	12.913	12.267	12.144	12.116	11.853	II
10	13 34 47.6856	−62 26.9472	G307.9219+00.0018	13.37	12.553	11.859	11.738	11.713	11.68	II
11	13 34 48.9096	−62 25.4874	G307.9283+00.0254	14.267	12.681	11.796	11.655	11.204	11.654	II
12	13 34 50.1048	−62 25.6944	G307.9300+00.0216	13.767	12.546	11.785	11.7	11.347	11.414	II
13	13 34 54.0384	−62 26.2866	G307.9358+00.0106	12.596	11.773	11.018	10.92	10.938	10.933	II
14	13 34 54.8448	−62 25.3746	G307.9399+00.0253	13.319	12.117	11.293	11.152	10.792	10.611	I-II
15	13 34 56.6544	−62 25.7538	G307.9422+00.0185	14.487	12.589	11.331	10.94	10.732	10.827	II
16	13 34 58.644	−62 26.6052	G307.9436+00.0039	13.376	12.672	12.142	11.819	11.508	11.403	I-II
17	13 35 0.6672	−62 25.641	G307.9502+00.0190	11.013	9.211	8.089	7.925	7.462	7.366	I-II
18	13 35 0.8784	−62 26.061	G307.9494+00.0121	13.54	12.424	11.79	11.598	11.264	11.535	II
19	13 35 4.7112	−62 25.1676	G307.9592+00.0255	13.87	12.348	11.382	11.22	10.892	10.994	II
20	13 35 5.0928	−62 24.3822	G307.9621+00.0383	14.298	13.186	12.453	12.352	12.217	12.064	II
21	13 35 5.5032	−62 26.2302	G307.9577+00.0078	12.143	10.783	9.836	9.826	9.511	9.568	II
22	13 35 7.9968	−62 25.6524	G307.9641+00.0165	14.241	12.207	10.879	10.721	10.298	10.135	I-II
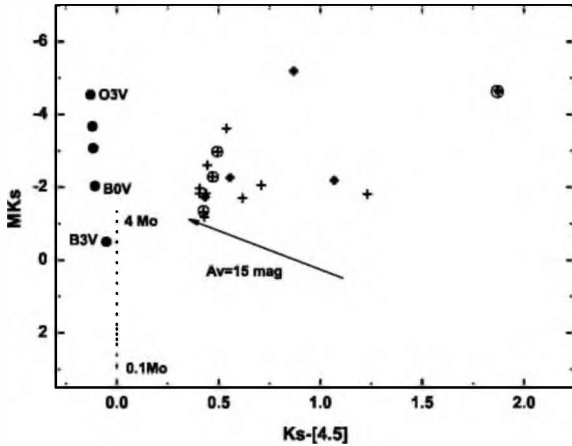
Fig. 10. Color–magnitude diagram for the SPITZER YSO candidates in the two selected regions near RA, Dec(J2000) = (13^{h}34^{m}30^s, −62°25′). Crosses and diamonds correspond to Class II and Class I-II objects, respectively. Main sequence stars from O3V to B3V (dots) and the isochrone for an age of 1 Myr (dotted line) are also plotted. The vector represents an absorption of 15 mag. The four sources shown as a cross inside a small circle are projected onto IR source B.

6. Discussion

6.1. Parameters of the gas

The distribution of the molecular gas and its comparison with that of the ionized gas indicates that the CO emission detected in the range −56 to −33 is probably related to the nebula. We note that Georgelin et al. (1988) proposed that the dust lane at Dec = −62°22′ is unconnected to RCW 78. However, the velocity of the molecular emission in this region, which coincides with the velocity of the ionized gas, casts doubts on this interpretation. Although we cannot discard Georgelin et al.'s interpretation, we believe that gas in the velocity interval mentioned above is linked to the nebula.

The mean H$_2$ column density N_{H_2}, the CO luminosity L_{CO}, the molecular mass M_{H_2} and a rough volume density n were derived separately for the molecular gas related to RCW 78 from the SEST and NANTEN data. The last data give more reliable values since the whole molecular cloud is included. Mean H$_2$ column densities were derived from ^{12}CO(1–0) data, by making use of the empirical relation between the integrated emission I_{CO} ($= \int T_{mb}dv$) and N_{H_2}. We adopted $N_{H_2} = 2.3 \times I_{CO} \times 10^{20}$ cm^{-2} (K km s^{-1})$^{-1}$ (Strong et al. 1988). The CO luminosities are defined as $L_{CO} = I_{CO} \times A$ (K km s^{-1} pc^2), where A is the area in pc^2. The mass includes a helium abundance of 10%.

From SEST data we obtained $N_{H_2} = 7.7 \times 10^{21}$ cm^{-2}. Adopting $d = 5 \pm 1$ kpc, $L_{CO} = (5.9 \pm 2.2) \times 10^3$ (K km s^{-1} pc^2) and $M_{H_2} = (3.0 \pm 1.2) \times 10^4$ $M_\odot$. The volume density $n \simeq 750 \pm 130$ cm^{-3} was estimated by distributing the molecular material within a region of 5′.1 in radius (7.4 pc at 5.0 kpc). The corresponding values derived from the NANTEN data are: $N_{H_2} = 6.6 \times 10^{21}$ cm^{-2}, $L_{CO} = (2.7 \pm 1.0) \times 10^4$ (K km s^{-1} pc^2) and $M_{H_2} = (1.3 \pm 0.5) \times 10^5$ $M_\odot$. A volume density $n \simeq 270 \pm 60$ cm^{-3} was estimated by distributing the molecular material within a region of 11′.8 in radius.

Optical depths were derived for two positions for which ^{13}CO profiles were obtained, assuming that the emission completely fills the SEST beam. The ^{12}CO and ^{13}CO profiles corresponding to one of these positions are shown in Fig. 10. The parameters of the Gaussian fitting to the CO components (peak temperatures T_p, central velocities V_{CO}, velocity width ΔV), and the integrated emission I_{CO} are listed in Table 2.

The peak optical depth of the ^{13}CO(2–1) lines were estimated from the peak T_{mb} values as $\tau(^{13}$CO[2–1]) $\simeq -\ln\{1 - T_{mb}(^{13}$CO[2–1])$/[10.58 \ J(T_{exc}) - 0.21]\}$, where $J(T_{exc}) = [e^{10.58/T_{exc}} - 1]^{-1}$. Excitation temperatures T_{exc} were derived from

13:33:10.9, −62:13:46

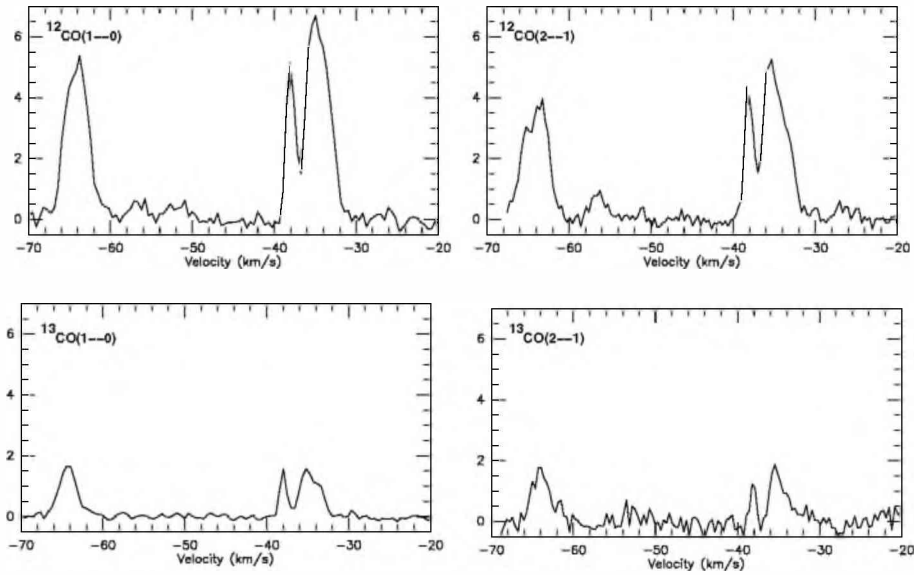**Fig. 11.** ^{12}CO and ^{13}CO SEST profiles corresponding to the position RA, Dec(J2000) = $(13^h 33^m 10.9^s, -62°13'46'')$. Line intensities are expressed as main-beam brightness temperature.

Table 2. Gaussian fitting to the CO profiles shown in Fig. 10.

Spectrum	T_p [K]	V_{CO} [km s^{-1}]	ΔV [km s^{-1}]	I_{CO} [K km s^{-1}]
^{12}CO(1–0)	5.3	−64.1	3.3	18.5
	0.5	−52.0	2.5	1.3
	5.2	−38.1	1.0	5.9
	6.7	−34.7	3.3	23.3
^{12}CO(2–1)	3.8	−64.0	3.6	13.7
	0.9	−56.5	2.1	1.9
	3.9	−38.2	1.0	3.9
	4.8	−35.0	3.6	17.7
^{13}CO(1–0)	1.7	−64.3	2.5	4.4
	1.4	−38.0	1.0	1.4
	1.5	−34.7	2.9	4.6
^{13}CO(2–1)	0.9	−63.9	2.6	2.6
	0.8	−38.1	0.7	0.6
	0.9	−35.1	2.2	2.2

the ^{12}CO(2–1) line assuming LTE and that ^{12}CO(2–1) is optically thick. Peak optical depths of the ^{12}CO lines were obtained as $\tau(^{12}CO) = [\nu(^{13}CO)/\nu(^{12}CO)]^2 [\Delta v(^{13}CO)/\Delta v(^{12}CO)] [^{12}CO]/[^{13}CO] \tau(^{13}CO)$; where v is the frequency of each transition, Δv is the FWHM of the observed line and $[^{12}CO]/[^{13}CO] = 70$ is the isotope ratio (Langer & Penzias 1990). T_{exc} in these regions are about 5–10 K, while optical depths $\tau(^{12}CO) \simeq 9$–24.

The intensity ratios ^{12}CO)/^{13}CO) for the different molecular components present in the two positions vary from 4.2 to 5.0 for the CO(1–0) lines and from 5.3 to 8.1 for the CO(2–1) lines. These ratios are similar to that found in Galactic molecular clouds (Castets et al. 1990).

The CO(2–1)/CO(1–0) ratios can give us information on the physical conditions of the gas. This ratio is more sensitive to gas density than kinetic temperature (Radford et al. 1991). We are aware, however, that these lines are optically thick. In order to extract the physical conditions of the observed area one can use the LVG approximation (Castets et al. 1990). To

determine the ^{12}CO(2–1)/^{12}CO(1–0) ratio, we convolve the CO(2–1) spectrum to the CO(1–0) resolution. The ratios obtained range between 0.6 to 0.8 and are consistent with low ratio gas (LRG), usually subthermally excited, with kinetic temperatures of about 10 K and densities $n_{H_2} < 1 \times 10^3$ cm^{-3}. Ratios of about 1 to 1.2 imply kinetic temperatures of about 20 K or larger, and densities $n_{H_2} > 1 \times 10^3$ cm^{-3}, which are not found (Sakamoto et al. 1994, 1997).

The parameters of the ionized gas can be estimated from the radio continuum image. A flux density $S_{4.85\,GHz} = 2.8$ Jy was derived from the image at 5 GHz. Adopting an electron temperature of 9000 K, the rms electron density n_e obtained from the expressions by Mezger & Henderson (1967) is in the range 4–9 cm^{-3}. To estimate this value we have assumed a spherical H II region with constant electron density. A rough estimate of the filling factor f can be obtained by taking into account the higher electron density derived from line ratios ($n'_e < 100$ cm^{-3}, Esteban et al. 1990) or the shell parameters around RCW 78. From the former method, we obtained a filling factor $f = (\frac{n_e}{n'_e})^{0.5} = 0.3$. Adopting an outer radius $R_s = 15' = 22$ pc (at 5.0 kpc) and a inner radius $R_i = 10' = 15$ pc (at 5.0 kpc), and assuming that 50% of the surface of the H II region is covered by plasma, $f = 0.4$. The electron density and ionized mass for $f = 0.3$–0.4 are in the range 6–15 cm^{-3} and $(3-5) \times 10^3$ $M_\odot$, respectively. The presence of He II was considered by multiplying the H II mass by 1.27. For the adopted distance uncertainty, the error in the ionized mass is about 40%.

The number of UV photons necessary to ionize the gas log $N_{Ly-c} = 49.3$. The comparison with the UV photon flux emitted by a WN7 is log $N_* = 49.4$ (Crowther 2007), suggesting that the WR star can maintain the gas in RCW 78 ionized.

6.2. Energetics

The dynamical age of a wind blown bubble can be estimated as $t_d = 0.56 \times 10^6 R/v_{exp}$ yr (McCray 1983), where R is the radius of the bubble (pc), v_{exp} is the expansion velocity (km s^{-1}), and the coefficient is the deceleration parameter. The constant is a

mean value between the energy and the momentum conserving cases. Adopting $R = 22$ pc and assuming a rather low value of 5 km s^{-1} for the expansion velocity (since no signs of expansion were found from optical and radio data), $t_d = 2.4 \times 10^6$ yr, suggesting that the O-type star progenitor of the WR star has contributed in shaping the bubble.

The comparison of the stellar wind mechanical energy $E_w (= L_w t_d = \dot{M} V_w^2 t_d/2)$ released by WR 55 and the kinetic energy of the interstellar bubble $E_k = M_b v_{exp}^2/2$ allows us to investigate if the stellar winds are capable of blowing the bubble.

To estimate E_w we adopt a conservative mass loss rate $\dot{M} \approx (1-3) \times 10^{-5}$ $M_\odot$ yr^{-1} (Nugis & Lamers 2000; Cappa et al. 2004), a terminal wind velocity $V_w = 1100$ km s^{-1} (see Sect. 1), and a dynamical age $t_d = 5 \times 10^5$ yr, compatible with the duration of the WR phase. The contribution of the O-type phase of the star was estimated adopting the mean values $\dot{M} = 2 \times 10^{-6}$ $M_\odot$ yr^{-1}, $V_w = 1500$ km s^{-1} (Prinja et al. 1990; Lamers & Leitherer 1993), and that the stellar wind acted for at least 2×10^6 yr. The wind mechanical energy released during the WR phase of the star is in the range $(0.6-1.8) \times 10^{50}$ erg, while for the O-star phase a value of 0.9×10^{50} erg is derived. The total energy released through stellar winds is in the range $(1.5-2.7) \times 10^{50}$ erg.

To estimate the kinetic energy of the interstellar bubble E_k we take into account the molecular mass alone since it is two orders of magnitude higher than the ionized mass. For the adopted expansion velocity, we obtained $E_k = 0.3 \times 10^{50}$ erg. The comparison between the kinetic energy of the nebula and the mechanical energy of the stellar wind is compatible with an interstellar bubble interpretation.

6.3. Star formation process

The presence of star formation activity in the environs of the nebula suggests that it may have been triggered by the expansion of the bubble. Indeed, active star forming regions are present at the periphery of many H II regions, where star fomation activity is triggered by the expansion of H II regions through the "collect and collapse" or the Radiative Driven Implosion models (e.g. Deharveng et al. 2005, and references there in).

The "collect and collapse" model indicates that expanding nebulae create compressed layers where gas and dust are piled-up between the ionization and the shock front. This dense layer fragments, forming molecular cores where new stars born. Whitworth et al. (1994) developed an analytical model useful to characterize the dense fragments in different scenarios. For the case of stellar wind bubbles, the model predicts the time at which the fragmentation occurs, t_{frag}, the size of the bubble at that moment, R_{frag}, the mass of the fragments, M_{frag}, and their separation along the compressed layer, r_{frag}. The parameters required to derive these quantities are the mechanical luminosity of the wind, L_w, the ambient density of the surrounding medium into which the bubble expands, n_0, and the isothermal sound speed in the shocked gas, a_s, which is supposed to be constant. The analytical expressions derived by Whitworth et al. are:

$$t_{frag} \ [10^6 \ \text{yr}] = 0.9 \ a_{.2}^{5/8} \ n_3^{-1/2} \ L_{37}^{-1/8} \tag{1}$$

$$R_{frag} \ [\text{pc}] = 9.6 \ a_{.2}^{3/8} \ n_3^{-1/2} \ L_{37}^{1/8} \tag{2}$$

$$M_{frag} \ [M_\odot] = 9.8 \ a_{.2}^{29/8} \ n_3^{-1/2} \ L_{37}^{-1/8} \tag{3}$$

$$2r_{frag} \ [\text{pc}] = 0.31 \ a_{.2}^{13/8} \ n_3^{-1/2} \ L_{37}^{-1/8} \tag{4}$$

where $a_{.2}$ is equal to a_s in units of 0.2 km s^{-1}, n_3 is the ambient density in units of 1000 cm^{-3}, and L_{37} is L_w in units of

10^{37} erg s^{-1}. a_s is an important factor to derive the parameters, while n_0 has a lower contribution, and the dependence on L_w is weak.

Taking into account the stellar wind parameters corresponding to the main sequence and WR phases of WR 55, and using the time during which the wind acted, we estimated $L_{37} = (0.20-0.35)$. Adopting $n_0 = 300$ cm^{-3} and $a_s = 0.2$ km s^{-1}, we obtained $t_{frag} \simeq 1.4 \times 10^6$ yr, $R_{frag} = 15$ pc, $M_{frag} = 15$ $M_\odot$, and $r_{frag} = 0.25$ pc.

For this interstellar bubble, the radius $R = 22$ pc and the dynamical age $t_d = 2.4 \times 10^6$ yr (see Sect. 6.1), and, consequently, $R_{frag} < R$ and $t_d > t_{frag}$, suggesting that the bubble is old enough for massive molecular fragments to form. Submillimetre continuum data may help to detect these fragments.

Pieces of evidence for the "collect and collapse" process are the presence of a dense shell surrounding the ionized region and star formation activity at the periphery of the ionized gas. The SEST data revealed that molecular gas surrounds the brightest section of the nebula (see Sect. 3.2). However, neither signs of strong gas compression nor star formation activity are detected at the periphery of this section of the nebula, as is the case in some H II regions (e.g. Zavagno et al. 2006; Deharveng et al. 2008). The NANTEN data showed that most of the molecular material appears projected onto the nebula (see Sect. 3.3). Although clear evidence of star formation activity seems to be related to this material, the face-on geometry makes it difficult to find observational evidence in favor of the "collect and collapse" process.

Star formation can also be triggered through the "radiation-driven implosion" (RDI) model, theorically developed by Lefloch & Lazareff (1994). Pillars or elephant trunks and cometary globules provide observational evidence of this process (e.g. Thompson et al. 2004; Urquhart et al. 2007). An inspection of the SuperCOSMOS Hα does not allow us to identify these objects. The image at 8 μm suggests that this kind of object might be present. High resolution molecular line observations are needed to investigate the nature of these small features.

Presently, neither of the two processes can be discarded to explain the star formation activity in the environs of RCW 78.

7. Conclusions

We have investigated the distribution of molecular gas related to the ring nebula RCW 78 around the WR star HD 117688 based on observations of ^{12}CO(1–0) and ^{12}CO(2–1) lines obtained using the SEST. Complementary molecular data from the NANTEN survey, H I data from the SGPS, and IRAS and radio continuum images were also analyzed.

The analysis of the SEST and NANTEN CO data reveals the existence of molecular gas with velocities in the range −56 to −33 km s^{-1} interacting with the western section of the nebula. The bulk of the emission is concentrated in two structures having velocities in the range −52.5 to −43.5 km s^{-1} and −43.5 to −39.5 km s^{-1}, coincident with the velocities of the Hα line. Based on morphological and kinematical evidence, we conclude that the arc-like structure with a velocity of −52.5 to −43.5 km s^{-1} is clearly associated with RCW 78. The feature with a velocity from −43.5 to −39.5 km s^{-1} is most probably related to the nebula. On the contrary, CO emission linked to the eastern section of the nebula is difficult to identify.

The radio continuum emission distribution at 4.85 GHz shows a shell-like feature, which resembles the Hα emission distribution.

The H I emission distribution shows a low emission region coincident in position with molecular gas with similar velocities,

suggesting that most of the neutral gas in this region is H_2. In this scenario, part of the neutral atomic gas encircling the depression might correspond to the envelope of the molecular cloud.

The distribution of the molecular and ionized gas is compatible with a scenario in which the ionized gas originated through photodissociation and ionization of the parental molecular cloud. The shell-like appearance of the ionized gas is suggestive of the action of stellar winds, which swept-up the surrounding gas, shaping an interstellar bubble. The lack of dense gas towards the east favored the expansion of the nebula in this direction. The proposed scenario also explains the off center location of WR 55.

As regards star formation activity towards RCW 78, the analysis of the IRAS, MSX, and Spitzer point source catalogues revealed the existence of two active star forming regions liked to the molecular gas associated with the nebula. The influence of the expansion of RCW 78 on the onset of star formation in these regions cannot be discarded.

The comparison between the wind mechanical energy released by WR 55 and its massive progenitor and the kinetic energy of the interstellar bubble indicates that the stellar wind of this star is capable of blowing the interstellar bubble. Thus, WR 55 is not only responsible for the ionization of the gas in the nebula but also for the creation of the interstellar bubble.

References

Benjamin, R. A., Churchwell, E., Babler, B. L., et al. 2003, PASP, 115, 953
Booth, R. S., Delgado, G., Hagstrom, M., et al. 1989, A&A, 216, 315
Brand, J., & Blitz, L. 1993, A&A, 275, 67
Cappa, C. E. 2006, Rev. Mex. A. A., 26, 9
Cappa, C. E., Rubio, M., & Goss, W. M. 2001, AJ, 121, 2664
Cappa, C. E., Goss, W. M., & Pineault, S. 2002, AJ, 123, 3348
Cappa, C. E., Goss, W. M., & van der Hucht, K. A. 2004, AJ, 127, 2885
Cappa, C. E., Niemela, V., Martín, M. C., & McClure-Griffiths, N. M. 2005, A&A, 436, 155
Castets, A., Duvert, G., Dutrey, A., et al. 1990, A&A, 234, 469
Chavarría, L. A., Allen, L. E., Hora, J. L., Brunt, C. M., & Fazio, G. G. 2008, ApJ, 682, 445
Chu, Y.-H. 1981, ApJ, 249, 195
Chu, Y.-H., & Treffers, R. R. 1981, ApJ, 250, 615
Chu, Y.-H., Treffers, R. R., & Kwitter, K. B. 1983, ApJS, 53, 937
Churchwell, E., Povich, M. S., Allen, D., et al. 2006, ApJ, 649, 759
Cichowolski, S., Pineault, S., Arnal, E. M., et al. 2001, AJ, 122, 1938
Comerón, F., Schneider, N., & Russeil, D. 2005, A&A, 433, 955
Condon, J. J., Griffith, M. R., & Wright, A. E. 1993, AJ, 106, 1095

Conti, P. S., & Vacca, W. D. 1990, AJ, 100, 431
Cooper, R. L., Guerrero, M. A., Chu, Y.-H., Chen, C.-H. R., & Dunne, B. C. 2004, ApJ, 605, 751
Crowther, P. A. 2007, ARA&A, 45, 177
Crowther, P. A., Hadfield, L. J., Clark, J. S., Negueruela, I., & Vacca, W. D. 2006, MNRAS, 372, 1407
Cutri, R. M., Skrutskie, M. F., van Dyk, S., et al. 2003, The IRSA 2MASS All-Sky Point Source Catalog, NASA/IPAC Infrared Science Archive
Cyganowski, C. J., Whitney, B. A., Holden, E., et al. 2008, AJ, 136, 2391
Deharveng, L., Zavagno, A., & Caplan, J. 2005, A&A, 433, 565
Deharveng, L., Lefloch, B., Kurtz, S., et al. 2008, A&A, 482, 585
Egan, M. P., Price, S. D., Moshir, M. M., et al. 1999, The Midcourse Space Experiment Point Source Catalog Version 1.2 Explanatory Guide, AFRL-VS-TR-1999-1522, Air Force Research Laborartory
Elmegreen, B. G. 2000, ApJ, 530, 277
Esteban, C. 1993, PASP, 105, 320
Esteban, C., Vilchez, J. M., Manchado, A., & Edmunds, M. 1990, A&A, 227, 515
Flaherty, K. M., Pipher, J. L., Megeath, S. T., Winston, E. M., & Gutermuth, R. A. 2007, ApJ, 682, 445
Freyer, T., Hensler, G., & Yorke, H. W. 2003, ApJ, 594, 888
Freyer, T., Hensler, G., & Yorke, H. W. 2006, ApJ, 638, 262
Georgelin, Y. M., Boulesteix, J., Georgelin, Y. P., Le Coarer, E., & Marcelin, M. 1988, A&A, 205, 95
Hamann, W. R., Koesterke, L., & Wessolowski, U. 1993, A&A, 274, 397
Junkes, N., Fürst, E., & Reich, W. 1992, A&A, 261, 289
Johansson, L. E. B., Greve, A., Booth, R. S., et al. 1998, A&A, 331, 857
Koenig, X. P., Allen, L. E., Gutermuth, R. A., et al. 2008, ApJ, 688, 1142
Lada, C. J. 1987, in Star forming regions, IAU Symp., 115, 1
Lada, C. J., Lada, E. A., Clemens, D. P., & Bally, J. 1994, ApJ, 429, 694
Lamers, H. J. G. L. M., & Leitherer, C. 1993, ApJ, 412, 771
Langer, W. D., & Penzias, A. A. 1990, ApJ 357, 477
Lefloch, B., & Lazareff, B. 1994, A&A, 289, 559
Lumsden, S. L., Hoare, M. G., Oudmaidjer, R. D., & Richards, D. 2002, MNRAS, 336, 621
Marshall, D. J., Robin, A. C., Reylé, C., Schultheis, M., & Picaud, S. 2006, A&A, 453, 635
McClure-Griffiths, N. M., Dickey, J. M., Gaensler, B. M., et al. 2005, ApJS, 158, 178
McCray, R. 1983, Highlights of Astron., 5, 567
Mezger, P. D., & Henderson, A. P. 1967, ApJ, 147, 471
Muzerolle, J., Allen, L. E., Fazio, G. G., & Lada, C. J. 1987, IAU Symp., 115, 1
Niedzielski, A., & Skorzynski, W. 2002, AcA, 52, 81
Nugis, T., & Lamers, H. J. G. L. M. 2000, A&A, 360, 227
Oey, M. S. 1996, ApJ, 467, 666
Parker, Q. A., Phillipps, S., Pierce, M. J., et al. 2005, MNRAS, 362, 689
Price, S. D., Egan, M. P., Carey, S. J., Mizuno, D., & Kuchar, T. 2001, A&A, 121, 2819
Prinja, R. K., Barlow, M. J., & Howarth, I. D. 1990, ApJ, 361, 607
Radford, S. J. E., Solomon, P. M., & Downes, D. 1991, ApJ, 368, L15
Rieke, G. H., & Lebofsky, M. J. 1985, ApJ, 288, 618
Rizzo, J. R., Martín-Pintado, J., & Desmurs, J. F. 2003, in A Massive Star Odyssey, from Main Sequence to Supernova, ed. K. A. van der Hucht, & C. Esteban, IAU Symp., 212, 742
Rochowicz, K., & Niedzielski, A. 1995, AcA, 45, 307
Sakamoto, S., Hayashi, M., & Hasegawa, T. 1994, ApJ, 425, 41
Sakamoto, S., Hasegawa, T., Handa, T., Hayashi, M., & Oka, T. 1997, ApJ, 486, 276
Siess, L., Dufour, E., & Forestini, M. 2000, A&A, 358, 593
Simon, J. D., Bolatto, A. D., Whitney, B. A., et al. 2007, ApJ, 669, 327
Stahler, S. W., & Palla, F. 2005
Strong, A. W., Bloemen, J. B. G. M., Dame, T. M., Grenier, I. A., et al. 1988, A&A, 207, 1
Thompson, M. A., White, G. J., Morgan, L. K., et al. 2004, A&A, 414, 1017
Turner, D. G., & Forbes, D. 2005, PASP, 117, 967
Urquhart, J. S., Thompson, M. A., Morgan, L. K., et al. 2007, A&A, 467, 1125
van der Hucht, K. A. 2001, New Astron. Rev., 45, 135
Walborn, N. 1982, AJ, 87, 1300
Watson, C., Povich, M. S., Churchwell, E. B., et al. 2008, ApJ, 681, 1341
Watson, C., Corn, T., Churchwell, E. B., et al. 2009, ApJ, 694, 546
Whitworth, A. P., Bhattal, A. S., Chapman, S. J., Disney, M. J., & Turner, J. A. 1994, MNRAS, 268, 291
Zavagno, A., Deharveng, L., Comeron, F., et al. 2006, A&A, 446, 171
Zavagno, A., Pomares, M., Deharveng, L., et al. 2007, A&A, 472, 835